



OPEN

## Research on ground pressure control modes in a subsea mine by physical model test and numerical simulation analysis

Weijun Liu<sup>1</sup>, Zhixiang Liu<sup>1</sup>, Jiadong Qiu<sup>2</sup>, Tengfei Guo<sup>2</sup> & Quanqi Zhu<sup>1</sup>✉

To solve the problems of deep mining safety and ground pressure control in Sanshandao gold mine, a novel ground pressure control mode of deep mining in a subsea metal mine was studied by physical model test and numerical simulation analysis. First, the novel ground pressure control mode was studied by physical model test, the surface deformation characteristics of the physical model were observed by the DIC method, and the deformation and damage characteristics of the rock layer were obtained. Then, the numerical simulation analysis of the novel ground pressure control mode was carried out and verified with the results of the physical model test. Finally, the determined ground pressure control model was verified by engineering. The research results show that the physical model has an obvious disturbance to the surrounding area during the excavation process according to the analysis of the strain monitoring points, and the strain value at the monitoring point was maintained at approximately one ten-thousandth. Meanwhile, the stress change reflected by the strain was consistent with the numerical simulation results, confirming the authenticity of the physical model test results. Additionally, the field industrial test shows that the control mode has a good control effect on the high ground stress in the deep subsea metal mining.

**Keywords** Ground pressure control, Physical model test, Numerical simulation analysis, Subsea metal mine

### List of symbols

DIC	Digital image correlation
$L_p$	the actual quarry size of the project
$K_L$	Geometric ratio
$L_m$	the dimensions of similar material models
$K_\rho$	Density similarity ratio
$\rho_p$	Density of the actual rock mass of the project
$\rho_m$	Density of similar material
$K_{\sigma_s}$	Stress similarity ratio
$\rho_p$	Stress on the actual rock mass of the project
$\rho_m$	Stress on similar material model
$\sigma_{\max}$	The maximum horizontal principal stress
$\sigma_{\min}$	Minimum horizontal principal stress
$\sigma_z$	Vertical stress
H	The burial depth of the measurement point
$\varepsilon_x$	Horizontal strain
$\varepsilon_h$	Vertical strain
$\varepsilon_{\max}$	The maximum principal strain
$\varepsilon_{\min}$	The minimum principal strain

<sup>1</sup>School of Resources and Safety Engineering, Central South University, Changsha 410083, China. <sup>2</sup>School of Resources, Environment and Safety Engineering, University of South China, Hengyang 421001, China. ✉email: quanqi\_zhu@csu.edu.cn

With the increasing difficulty of mining deep mineral resources, coastal and continental shelf sea-based metal mines have now become a new direction for mineral resource mining in China<sup>1–3</sup>. According to statistical data, there are fewer metal mines mined on the seabed in the world, mainly in Newfoundland iron ore in Canada, Kruva iron ore in Finland, the Levant tin mine in the UK, and the Sanshandao gold mine in China<sup>4</sup>. However, subsea metal ore mining is deep mining. Due to the complex mining environment it faces, coupled with external dynamic disturbances, it may induce geological hazards and safety problems such as large-scale rock explosions in the mining area, fault slip, rock movement deformation, and sudden water, so how to safely and efficiently mine deep subsea metal ore has been a difficult problem<sup>5,6</sup>. It has been documented that in-situ stress levels in certain deep-sea mining areas, including the Clarion-Clipperton Fracture Zone, can attain 40–60 MPa, representing a high-risk environment for rockburst<sup>7</sup>. The severe implications of such geo-stresses are illustrated by the Mponeng Gold Mine in South Africa, where at approximately 3,000 m depth, stresses surpass 100 MPa and have been associated with several hundred rockburst events over the lifecycle of an individual stope<sup>8</sup>. Furthermore, substantial water inflows present a parallel hazard, as observed at the West Rand Gold Field, where inflows of up to 80,000 m<sup>3</sup> per day resulted in complete mine flooding and caused irreversible impacts on regional groundwater regimes and surface stability<sup>9</sup>. Currently, subsea metal mines are usually mined by the filling method, and the differences in mining methods, recovery sequences and other factors are likely to affect the transfer of deep stresses and recreate the unloading environment, which in turn results in different ways of regulating deep ground pressure in subsea metal mines. Therefore, the selection of a reasonable ground pressure control mining method is of great research significance for deep mining<sup>10,11</sup>.

Recently, relevant research on the ground pressure control aspects of deep mining has been conducted by numerous scholars, and the common research methods are mainly theoretical analysis<sup>12</sup>, numerical simulation analysis<sup>13,14</sup> and physical model tests<sup>15,16</sup>. For example, Qian et al.<sup>17</sup> used a numerical simulation analysis method to establish a geological model of highly inclined coal seams, predicted surface subsidence and set up safe mine pillars, which effectively controlled surface subsidence and surrounding rock damage. Wang et al.<sup>18</sup> applied the physical similarity model to study the surface settlement of mining in composite strata and summarized the movement characteristics and rules of roof settlement in various regions. To predict the ground settlement caused by deep mining, Li et al.<sup>19</sup> established a theoretical model for the prediction and analysis of dynamic settlement in deep mining by using a theoretical analysis model, and the comparison with the measured results showed that the model was effective. Zheng et al.<sup>20</sup> used a physical model test to obtain a bed separation grouting simulation. Cui et al.<sup>21</sup> utilized a physical model test to study the comparative analysis of energy release under different mining methods. Li et al.<sup>22</sup> carried out a similar material-physical model simulation of column instability damage in a slowly dipping medium-thick phosphate rock quarry, and the results showed that column damage exhibited a significant “domino effect”. Although the above research methods have achieved good results, they all have their own limitations. For example, although the theoretical analysis method can reveal the nature and law of the problem, it is mainly suitable for simple engineering problems, and it is not good for solving most complex engineering problems. Although the numerical simulation method has a high degree of flexibility and expansibility, there are several problems, such as calculation error and algorithm instability. Although the physical model test method has the directness and repeatability of the test, it may be affected by the experimental conditions and environment and has certain limitations. Because practical engineering problems are complex and changeable, a single method cannot fully reflect the actual effect. Therefore, more comprehensive, rich and reliable results can be obtained by using theoretical analysis, experimental analysis and numerical simulation analysis methods<sup>23</sup>.

To achieve a better research effect, many combinations of research methods have often been applied to analyze the ground pressure control of deep well mining by many scholars and have achieved better results<sup>24–26</sup>. For example, Xu et al.<sup>27</sup> proposed a ground pressure energy control scheme through engineering verification based on a physical model test and three-dimensional numerical simulation for the energy propagation problem caused by rock mass instability in a steep slope coal seam in the Urumqi mining area of Xinjiang. Wang et al.<sup>28</sup> used a physical model test and theoretical analysis to study the reasonable width of waterproof coal pillars and determined the optimal width of the pillars. Zhang et al.<sup>29</sup> studied the dynamic formation movement characteristics of open pit and underground combined mining through physical model tests and numerical simulation analysis and revealed the internal movement laws of rock strata. Lu et al.<sup>30</sup> used numerical simulation analysis and physical model tests to study the stability of the surrounding rock structure under filling mining of steeply inclined coal seams. Li et al.<sup>31</sup> used a physical model test to study the spatial distribution characteristics and evolution rules of the overlying water-conducting fault zone in deep coal mining. Zhang et al.<sup>32</sup> used a physical model test and numerical simulation analysis to study the stability of weakly consolidated water-bearing areas in coal mining and analyze the decompression effect of aquifers.

Therefore, considering the complexity of ground pressure control in deep subsea metal mining, the deformation characteristics of the physical model surface are observed by the DIC method by conducting a physical model test on the deep-960 middle mining area, and then a numerical model is established according to the engineering conditions of deep subsea mining in the Sanshandao gold mine. In addition, the test results of the physical model are compared and analyze with the numerical analysis results. Finally, the mining method is verified by field industrial tests of the ground pressure control mining method, which verifies the effectiveness and rationality of this ground pressure control method.

## Engineering background

The Sanshandao gold mine has three mining areas: Xinli, Xishan and Xiling. The current production is mainly in Xinli and Xishan, while Xiling is located 2 km east of Xishan, with the ore body's assigned elevation between –500 and –2600 m, which is a deep mining body and is currently in the infrastructure period. The specific location of the mine is shown in Fig. 1. The mining scale of the Xinli mine is 6,500 t/d, using the combined shaft + auxiliary

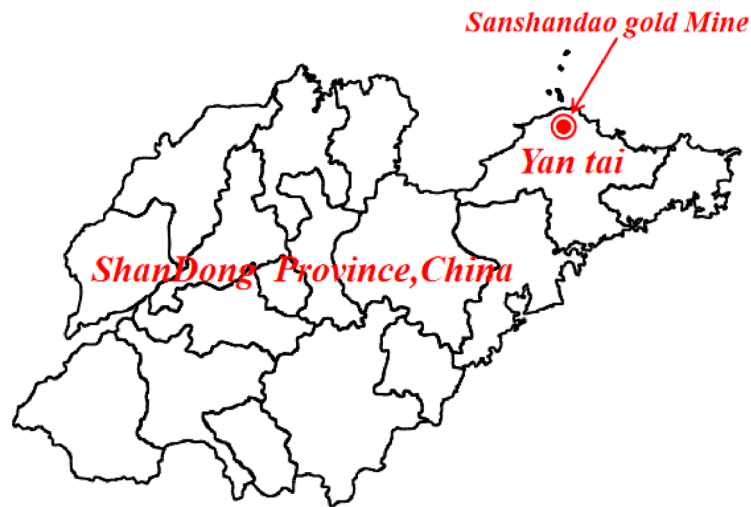


**Fig. 1.** The location of the mine.

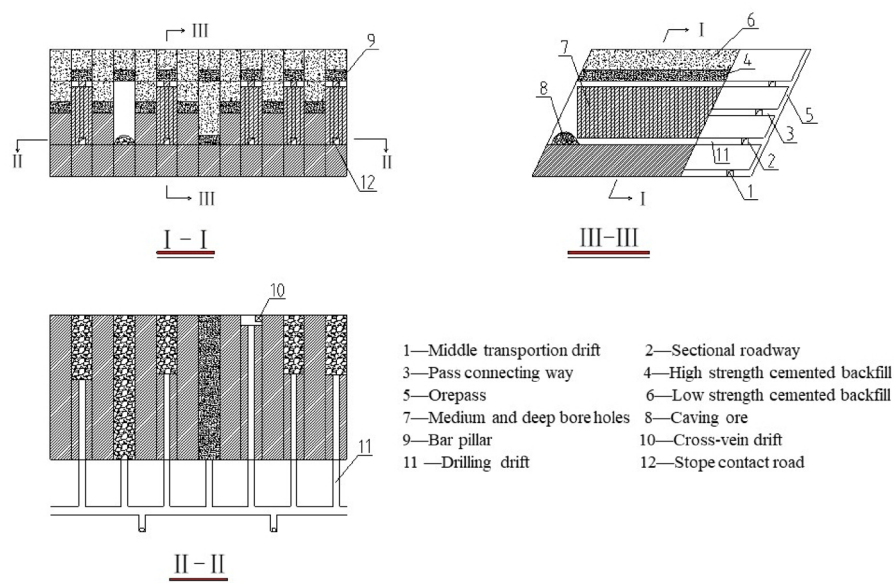


**Fig. 2.** Diagram of the mining methods used in the Xishan mining area.

ramp development method, and the mining method adopts the plate mechanized chamber-column cross-stratification filling mining method and mechanized upwards approach filling mining method. The diagram of mining method in Xishan mining area is shown in Fig. 2. After three phases of technical transformation, the mining scale of the Xishan mine is 1500 t/d, and the ramp has been extended to -960 m. Currently, the Xishan mine has been explored to the middle section of -960 m, and the deep mining of the Xishan mine faces a high-temperature, high-pressure and high-humidity operating environment and complicated mining technical conditions.

The deep ore body of the Xishan mining area has an average dip of 44° and a horizontal thickness of 40 m. The  $F_1$  fault is revealed in the middle of the ore body, and its production is basically the same as that of the ore body. The ore body of this fault is broken, which is a typical inclined thick and broken ore body. Based on geological investigations and rock mechanics tests, the upper plate is fractured serialized granitic rock, the ore body is fractured pyritic serialized granitic rock, and the lower plate is granite. The lithological stabilities of the upper and lower plates are different; moreover, the upper plate is a more broken and unstable ore body, and the lower plate is a stable ore body. A schematic diagram of the ore body and the  $F_1$  fault assignment is shown in Fig. 3.

In view of the mining technology characteristics of deep mining, large differences in the lithological stability of the upper and lower plates, high ground stress and obvious ground pressure, combined with the actual situation of the Xishan mine, based on the mining method of backfilling in the downwardsard direction after the segmentation of the upper and lower plates in the medium depth hole, a deep mining ground pressure control

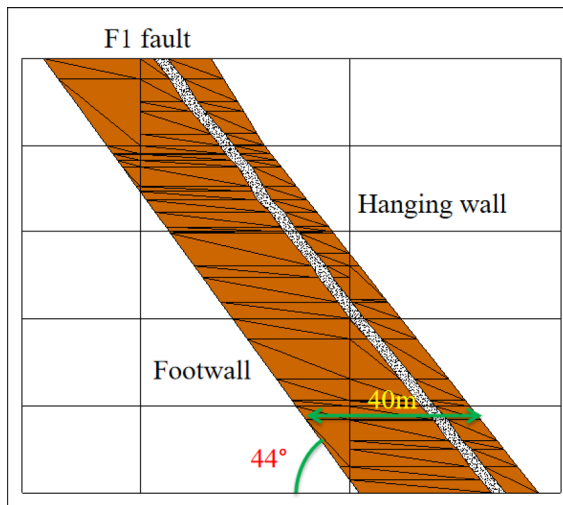


**Fig. 3.** Schematic diagram of the ore body and  $F_1$  fault assignment.

method was proposed. Therefore, for this mining ground pressure control method, a physical model test is carried out, and a physical model test is established. Additionally, relevant research on the mechanical behavior of the model is conducted during the excavation process.

### Physical model test

For the ground pressure control model of deep subsea metal mining, the model dimensions and excavation steps were simplified to facilitate physical model test<sup>33,34</sup>.

### Test system

In Fig. 4(a), the physical model test system consists of a test stand, a hydraulic servo pump station, horizontal and vertical pressure servo loading devices, a top water pressure servo loading device, a static strain test system, and a DIC. The static strain testing system includes strain gauges, testing hardware (strain signal conditioner, data collector), and professional testing and analysis software. The DIC is a method to measure the deformation by correlating the images taken before and after the deformation of the object, which has the advantages of noncontact, full field, and easy operation<sup>35–38</sup>.

The DIC system includes a high-speed camera, two light sources and a set of DIC analysis software. The high-speed camera has a shooting speed of 8 fps and a resolution of  $1344 \times 888$  pixels (1 pixel is approximately 0.22 mm). The physical model needs to be sprayed with white matte paint before the marker points, and the scattered marker points are sprayed with black matte paint. The scattered spot size is controlled at 3–4 mm, and the scattered spot spacing is 1.5 mm. The hydraulic servo loading device is composed of a hydraulic cylinder and pressure head, which can realize two loading modes of position control and force control and can apply horizontal and vertical load pressure to the model, and the maximum horizontal and vertical load is 300 kN. The hydraulic servo device applies water pressure directly to the top of the model through the combined action of vertical pressure and the hydraulic loading device.

### Principle of similarity

The design of similar ratios for similar materials includes parameters such as the geometric ratio, density, vertical stress, horizontal stress, Poisson's ratio, elastic modulus, tensile strength, and uniaxial compressive strength<sup>39–41</sup>. Equation (1) is the formula for the geometric similarity ratio.

$$K_L = \frac{L_p}{L_m} \quad (1)$$

where  $K_L$ ,  $L_p$ , and  $L_m$  are the geometric ratio, the actual stope size of the project, and the dimensions of similar material models, respectively.

Equation (2) is the density similarity ratio calculation method<sup>42–44</sup>.

$$K_\rho = \frac{\rho_p}{\rho_m} \quad (2)$$

where  $K_\rho$ ,  $\rho_p$ , and  $\rho_m$  are the density similarity ratio, the density of the actual rock mass of the project, and the density of the similar material model, respectively.

Equation (3) is the stress similarity ratio calculation.

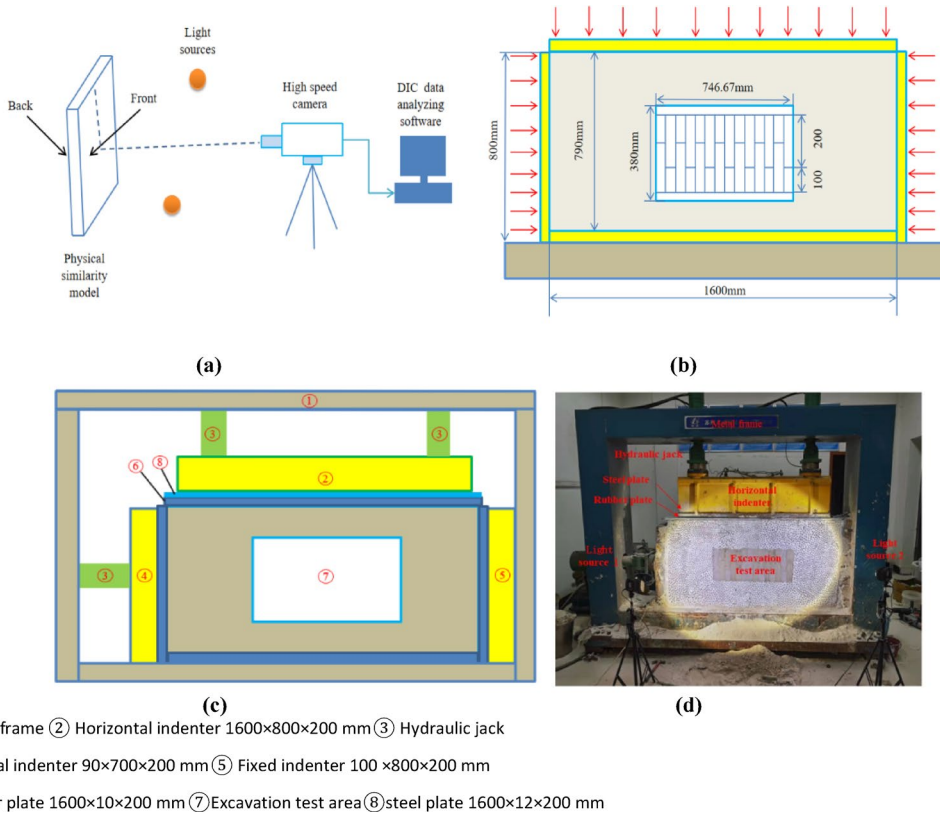


**Fig. 4.** The physical model test system: (a) schematic diagram of the DIC test system; (b) physical model diagram; (c) loading device diagram and boundary conditions; (d) physical model test system field diagram.

$$K_{\sigma s} = \frac{\sigma_{ps}}{\sigma_{ms}} = K_L K_\rho \quad (3)$$

where  $K_{\sigma s}$ ,  $\sigma_{ps}$ , and  $\sigma_{ms}$  are the stress similarity ratio, the stress on the actual rock mass of the project, and  $\sigma_{ms}$  is the stress on a similar material model, respectively.

By calculating and analyzing the ground stress data from multiple measurement points in each middle section of the Sanshandao mine, the regression characteristic Eq. (4) to (6) for the variations in  $\sigma_{\max}$ ,  $\sigma_{\min}$ , and  $\sigma_z$  with burial depth can be obtained, and the results are shown below:

$$\sigma_{\max} = 0.11 + 0.0539H \quad (4)$$

$$\sigma_{\min} = 0.13 + 0.0181H \quad (5)$$

$$\sigma_z = 0.08 + 0.0315H \quad (6)$$

where  $H$  is the burial depth of the measurement point, in m.

## Physical model test Preparation and steps

In the test process, the test model should first be constructed in the model box according to a certain similarity ratio and then loaded according to the predefined loading mode<sup>45–47</sup>.

Figure 4(b) and Fig. 4(c) show the physical model diagram and the physical model loading device schematic, respectively. As shown in Fig. 4(b), the model test bench is 2500 mm long and 2100 mm high, and it is in the form of a frame structure, which is welded by steel sections and has sufficient rigidity. A hydraulic cylinder for applying a horizontal force is fixed to the test frame column at one end, and two hydraulic cylinders for vertical loading are installed on the test frame beam at the top. The maximum model box size is 1600 mm in length, 800 mm in width and 200 mm in height. According to the situation of the Sanshandao gold mining process, the mining prototype in this experiment is a 112 m long and 45 m wide mining area, and some widths need to be reserved from the simulated mining area to the edges of both sides of the model. In addition, the geometric similarity ratio  $K_L = 150$  is used in this experiment, namely, the simulated excavation area with a central length of 746.67 mm and a width of 300 mm is selected in the similar model.

As shown in Fig. 4(c), the bottom of the water tank at the top of the physical model is not closed, and a rectangular hollow sealing rubber is fitted between the bottom of the water tank and the top of the model specimen. The seal rubber ring is 10 mm thick, as large as the bottom of the water tank, 1300 mm  $\times$  200 mm, and the rectangular hollow size is slightly smaller than the size of the top of the model specimen, 1100 mm  $\times$

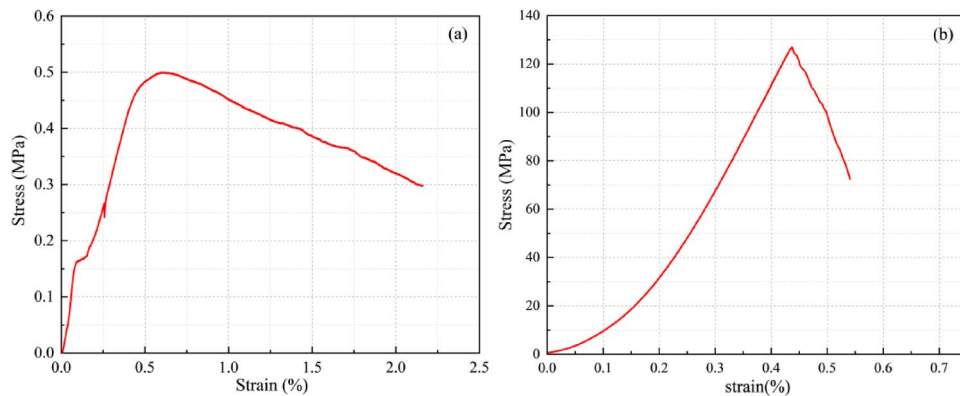


**Fig. 5.** Stress-strain curves of specimens: (a) the similar materials; (b) the orebody(granite).

Materials	Density	Elastic modulus	Compressive strength	Poisson's ratio
	/kg/m <sup>3</sup>	/GPa	/MPa	
Orebody(granite)	2638	36.94	80.0 ~ 126.95	0.24
Similar materials	1804	30.24	0.32 ~ 0.50	0.24

**Table 1.** Physical and mechanical properties of similar materials.

120 mm. The width of the ring band of the seal rubber ring is 30 mm, which is slightly larger than the thickness of the water tank wall to ensure that the water tank wall completely passes through the seal rubber ring on the top of the model and that the body of water inside the tank is directly on the top of the model. In this test, construction gypsum with quartz sand and water is taken as the raw material for the preparation of similar materials. According to a physical model test with construction gypsum and quartz sand as similar material raw materials, a quartz sand: gypsum ratio of 1:6 was configured with similar simulation material mechanical indexes: bulk density of 1.7–2.0 kN/m<sup>3</sup> and compressive strength of 0.4–2.2 MPa. According to the physical and mechanical indicators of the original rock at the site, the bulk weight is 2.6 kN/m<sup>3</sup>, and the compressive strength is 80–127 MPa. From formula (2) and formula (3), the density similarity ratio  $K_\rho$  is selected as 1.44. Therefore, the ratio of construction gypsum to quartz sand is selected as 1:6, and the prepared similar material has a bulk weight of 1.8 kg/m<sup>3</sup> and a compressive strength of 0.5 MPa. The similar materials can effectively simulate the failure behavior of rock masses. The Physical model test system field diagram is shown in Fig. 4(d). And the stress-strain curves of specimens are shown in Fig. 5. And the Physical and mechanical properties of similar materials is shown in Table 1.

In a physical model test, the prototype depth of the Sanshandao gold mining area was 960 m, and according to Eq. (4)~(6),  $\sigma_{\max}$  is 51.854 MPa,  $\sigma_{\min}$  is 17.506 MPa, and  $\sigma_z$  is 30.32 MPa. According to Eq. (3), the stress similarity ratio  $K_{\sigma s}$  is 216. According to the model similarity principle, the physical model should be subjected to a compressive force of 0.240. In the horizontal direction, the force area in the horizontal direction is 0.16 m<sup>2</sup>; namely, the equipment should apply a force of 38.4 kN in the horizontal direction of the model. Similarly, the vertical direction should be subjected to a compressive force of 0.140 MPa, and the force area in the vertical direction should be 0.32 m<sup>2</sup>; namely, the equipment should exert a force of 44.92 kN in the vertical direction of the model.

To better study and analyze the rock stability under the mining disturbance of the physical model, strain gauges were installed around the physical model test to verify the strain. In this experiment, a total of 16 strain gauges were designed and arranged around the physical model, numbered from 1 to 16, among which 5 strain gauges were arranged at the top of the model, numbered from 1 to 5, 6 at the side helpers, numbered from 6 to 8 for the left helper and 14 to 16 for the right helper, and 5 strain gauges were arranged at the bottom, numbered from 9 to 13, as shown in Fig. 6. Due to the strain gauges falling off at some locations (at 14 ~ 16) during the experiment, the actual arrangement of the strain gauges and excavation-filling sequence is shown in Fig. 6, with immediate filling after mining, followed by the next excavation step after filling, where the specific excavation-filling sequence is 1–12. The excavation-filling sequence diagram of the physics model test is shown in Fig. 7.

## Numerical simulation

FLAC3D is widely used to solve complex engineering problems<sup>48–50</sup>. For the mining process of the relatively solid ore body in the lower plate of the Sanshandao deep ore body by a medium-deep hole drop and subsequent filling mining method after splitting the upper and lower plates, a three-dimensional numerical model is established in this paper to explore the stress release in the back mining ground under this ground pressure control method and to study the effect of back mining ground pressure control.

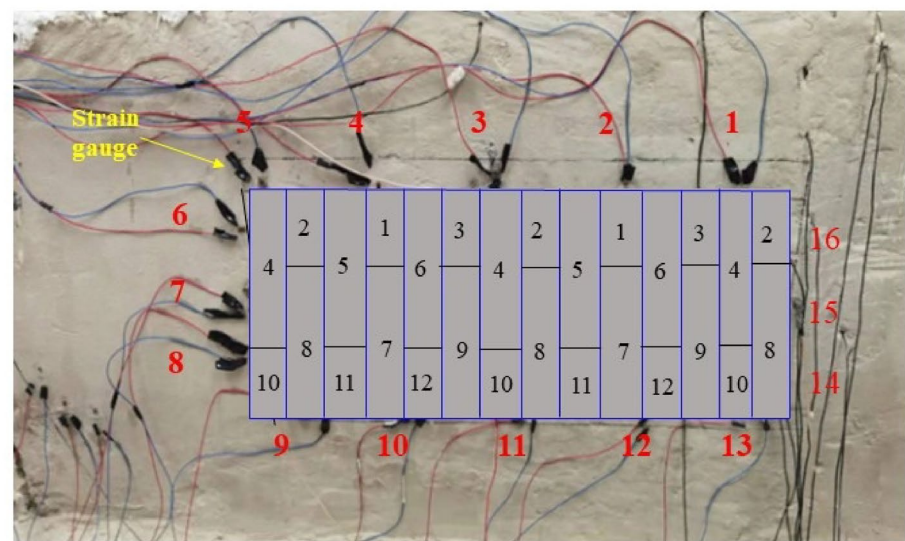


**Fig. 6.** Schematic diagram of the actual arrangement of the strain gauges and excavation scheme.



**Fig. 7.** Diagram of the excavation-filling sequence used in the physics model test.

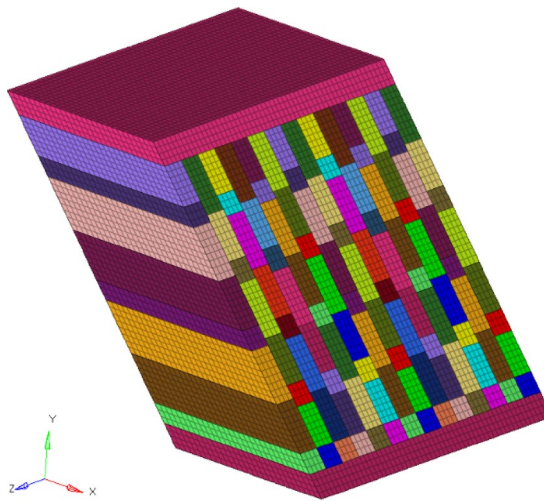


**Fig. 8.** Internal grouping and meshing of ore body.

Type	Elastic modulus E/Pa	Shear modulus E/Pa	Density g/cm <sup>3</sup>	Internal friction angle/Φ	Cohesion/Pa	Tensile strength /Pa
Upper bedrock	$1.096 \times 10^{10}$	$6.895 \times 10^9$	2700	36.94	$4.2778 \times 10^7$	$8.54 \times 10^6$
Bottom bedrock	$1.096 \times 10^{10}$	$6.895 \times 10^9$	2700	36.94	$4.2778 \times 10^7$	$8.54 \times 10^6$
Peripheral rock along the strike of the orebody	$1.096 \times 10^{10}$	$6.895 \times 10^9$	2700	36.94	$4.2778 \times 10^7$	$8.54 \times 10^6$
Orebody	$3.218 \times 10^9$	$2.024 \times 10^9$	2700	32.60	$2.145 \times 10^7$	$4.91 \times 10^6$
1:4 backfill body	$2.894 \times 10^7$	$2.449 \times 10^7$	2700	43.50	$3.1 \times 10^5$	$1.51 \times 10^6$
1:8 backfill body	$1.234 \times 10^7$	$9.71 \times 10^6$	2700	38.70	$1.71 \times 10^5$	$4.2 \times 10^5$
Noncollodion backfill	$6.32 \times 10^6$	$3.68 \times 10^6$	2700	32.00	$1.7 \times 10^4$	$3 \times 10^4$
Top Column	$2.894 \times 10^7$	$2.449 \times 10^7$	2700	43.50	$3.1 \times 10^5$	$1.51 \times 10^6$
Bottom column	$1.096 \times 10^{10}$	$6.895 \times 10^9$	2700	36.94	$4.2778 \times 10^7$	$8.54 \times 10^6$

**Table 2.** Mechanical parameters of the materials.

## Modelling

Due to the complexity of the deep mining site process of the Sanshandao gold mine subsea metal ore, the model was simplified. The established numerical model is 224 m in length along the vertical strike of the ore body and 174 m in the vertical direction with the ore body as the centre. The X direction has been selected as the vertical strike of the ore body, while the Y direction is vertical and the Z direction is along strike of the ore body. In the established stope model, fourteen chambers are arranged along the direction of the ore body. Each chamber is 8 m in width, 55 m in thickness, 87 m in height, and 6 m in the top and bottom columns. Moreover, a 3D numerical model was established, and the ore body model was divided into 130 groups, including 1 group of top columns, 1 group of bottom columns, and 128 groups in the ore body area. Finally, the ore body model is meshed again, 2 m is divided into a grid, and the computational grid model is shown in Fig. 8.

## Mechanical parameters of materials

The numerical analysis in this research was implemented with FLAC3D. The Mohr-Coulomb elastoplastic constitutive model was utilized to represent the rock mass, a model prevalent in geotechnical engineering for its capability to replicate both pre-yield elastic deformation and post-yield plastic failure. The yield criterion of the model is defined by the material's cohesion (c) and internal friction angle (Φ). And the mechanical parameters of the materials are shown in Table 1.

## Simulation of the excavation process

In the excavation process, stope number 1 was first mined and then immediately filled. Then, stope 2 was mined and immediately filled to complete the 18 mining steps, as shown in Fig. 9, to represent the model excavation sequence.

## Results and discussion

### Analysis of the physical model test results

The strain changes at the monitoring points of the top slab during the test are shown in Fig. 10. It can be concluded that the strains of monitoring points 1 and 5 decrease after the first filling is completed in steps 1 and 2, while the strains at monitoring point 3 continue to increase steadily. In the remaining 10 steps, the strain

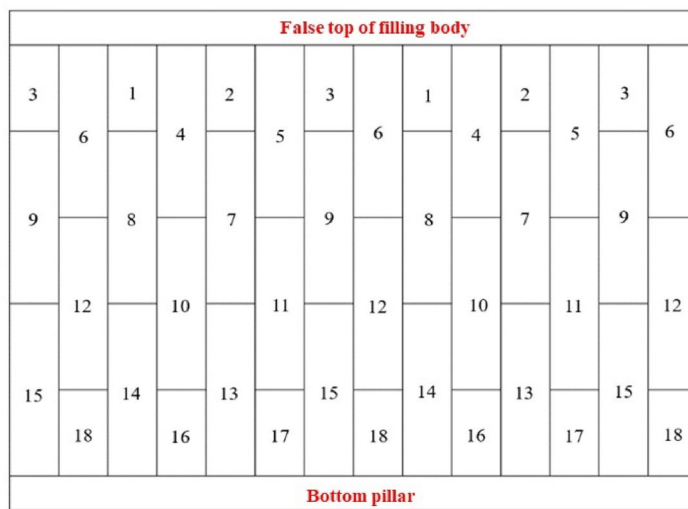


**Fig. 9.** Excavation sequence of the 3D numerical model.

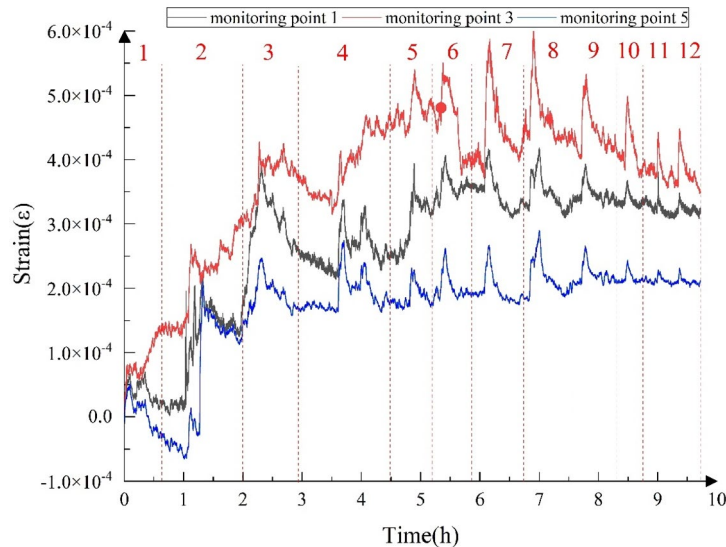


**Fig. 10.** Strain diagram of the top plate monitoring points during the whole excavation step.

patterns at the three monitoring points of the top slab are basically the same. During the excavation process, the strain increases significantly, while it remains relatively stable after filling, which proves the good effect of the filling body on ground pressure control. Its strain reaches the maximum value during the excavation process of step 7 and step 8, and the maximum strain values at the three monitoring points are  $4.2 \times 10^{-4}$ ,  $6 \times 10^{-4}$ , and  $2.9 \times 10^{-4}$ . In addition, it can be concluded that among the influences of the test on the strain of the rock mass in the roof, the influence on monitoring point 5 is higher than that on monitoring point 1, and the influence on monitoring point 1 is higher than that on monitoring point 5. It can be seen from the values that the test has minimal interference on the rock mass in the whole roof and will not cause damage.

The strain diagram of the lateral monitoring points during the whole process of the excavation step is shown in Fig. 11. Through the overall analysis of all the monitoring points, the change pattern of the strain curve of each monitoring point is similar, showing a low-high-low change pattern. The maximum strain value in each of these steps appeared after excavation when the exposed area was the largest. With the completion of filling, the expansion and supporting effect of the filling body decrease the strain. Among all monitoring points, the strain change of monitoring point 6 is the largest, indicating that excavation has the greatest impact on monitoring point 6. The strain change at monitoring point 8 is the smallest, indicating that the excavation has the least influence on monitoring point 8.

The strains of the bottom monitoring points during the whole excavation step with respect to the excavation time are shown in Fig. 12. Through the overall analysis of all the monitoring points, the change pattern of each

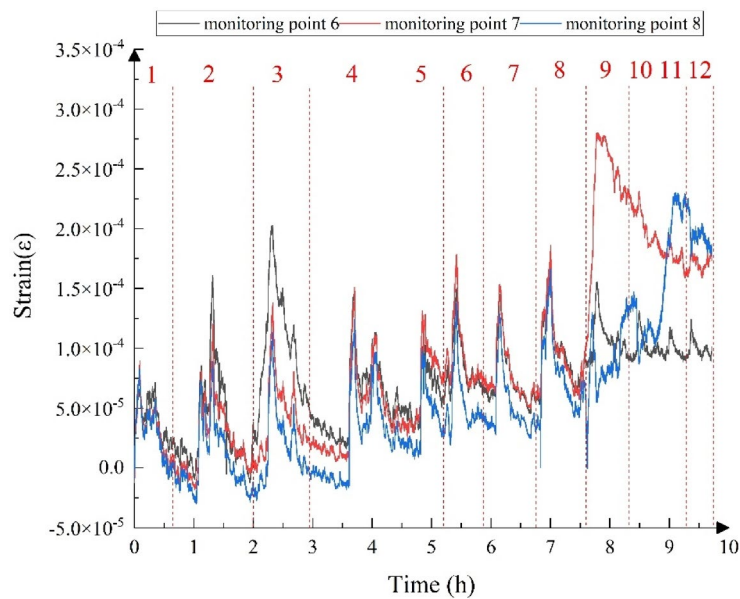


**Fig. 11.** Strain diagram of lateral monitoring points during the whole excavation process.

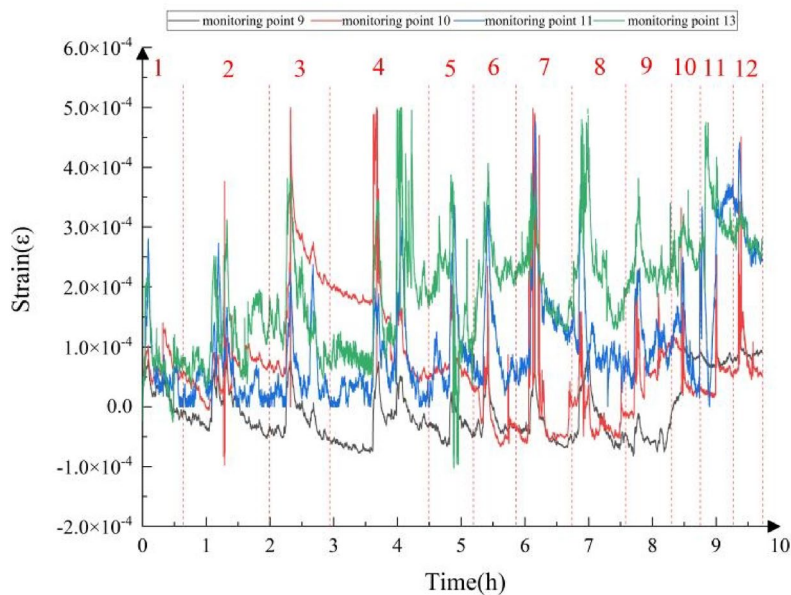


**Fig. 12.** Strain diagram of the bottom plate monitoring points during the whole excavation step.

monitoring point is similar, showing a low-high-low shape in each excavation step, and the maximum strain generally appears after excavation. With the completion of filling, the strain gradually decreased, but the overall trend increased. Among them, the strain change at monitoring point 13 is the largest, and the strain change at monitoring point 9 is the smallest, indicating that the excavation disturbance at monitoring point 13 is the largest and the disturbance at monitoring point 9 is the smallest.

#### The numerical simulation results analysis

**Vertical stress variation analysis** Figure 13 represents the vertical stress at excavation steps 1–9. When excavation is carried out, the stress concentration area is mainly concentrated in part of the excavated filled area, and as the excavation steps continue, the stress concentration phenomenon in part of the excavated filled area is lifted. During excavation steps 1–3, the top and bottom column stress concentration phenomenon is not obvious, and after excavation steps 4–6, the stress concentration area is smaller. As mining proceeds to steps 7–9, the stress

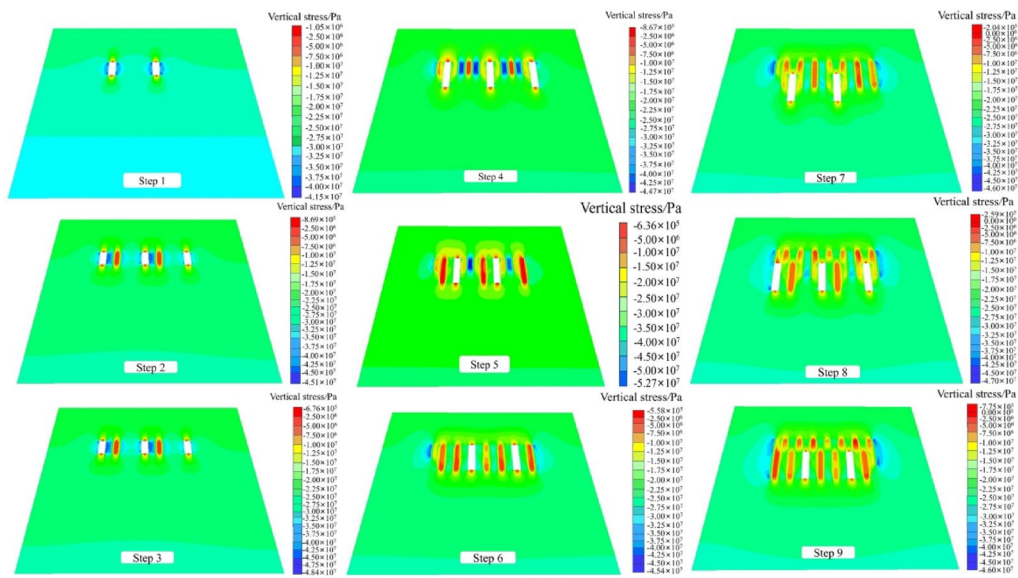


**Fig. 13.** Excavation steps 1–9 vertical stresses.

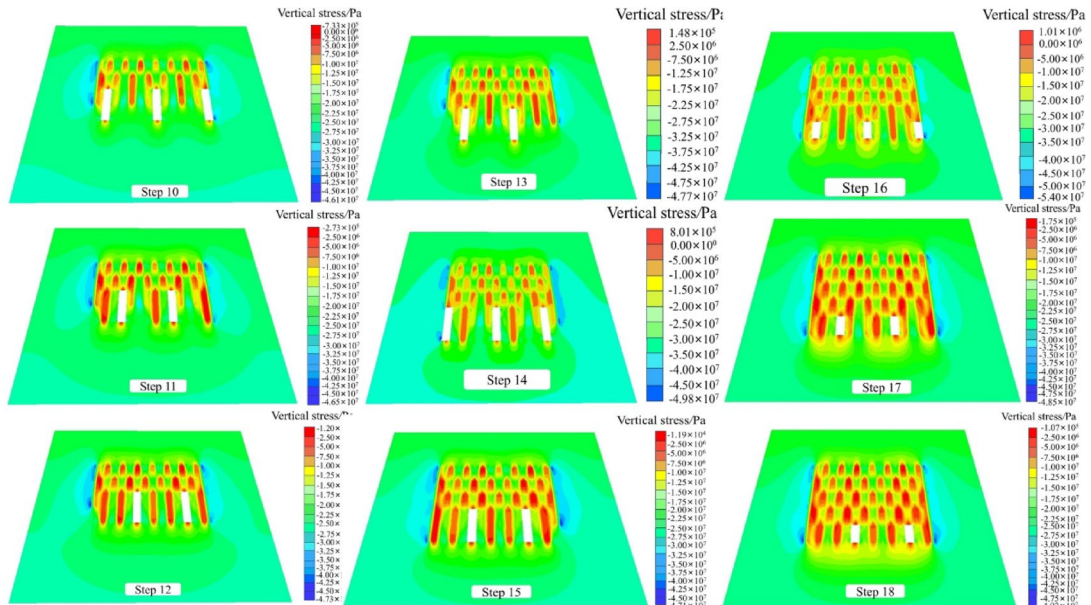


**Fig. 14.** Excavation steps 10–18 vertical stresses.

concentration phenomenon of the surrounding rock on both sides of the stope is further highlighted, and the stress concentration area continues to expand.

As shown in Fig. 14, the vertical stress concentration phenomenon is more serious in excavation steps 10–12, and upwards stress concentration occurs in the bottom plate of certain mine houses. In excavation steps 13–15, the vertical stress direction is vertically downwards, and the downwards deformation of the stope roof needs to be noted at this time. In addition, after backfilling in step 17 and mining in step 18, the stress concentration area of the peripheral rock on both sides of the ore body was reduced, showing a better effect of ground pressure control.

The vertical stress evolution calculation results show that the vertical stress is relatively small, the stress distribution is relatively uniform, the local stress concentration phenomenon is relatively insignificant, and the control effect of the ground pressure control method is relatively good.

**Horizontal stress variation analysis** The horizontal stress variation diagram of steps 1–9 of the excavation step is shown in Fig. 15. Figure 15 shows that with the progress of excavation steps 1–3, the horizontal stress concen-

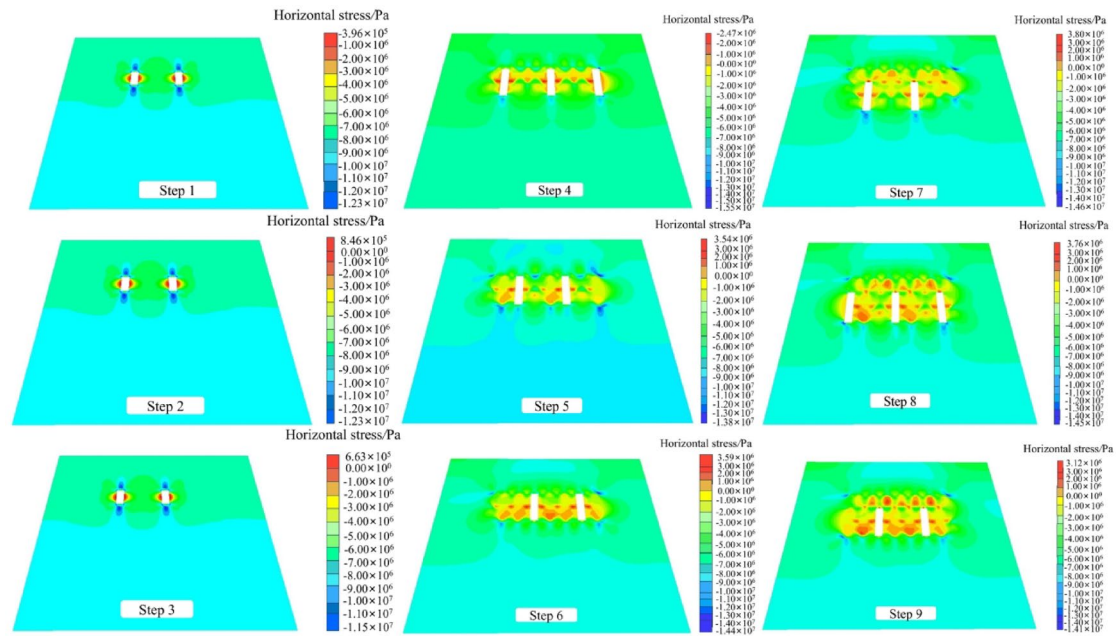


**Fig. 15.** Excavation steps 1–9 horizontal stresses.

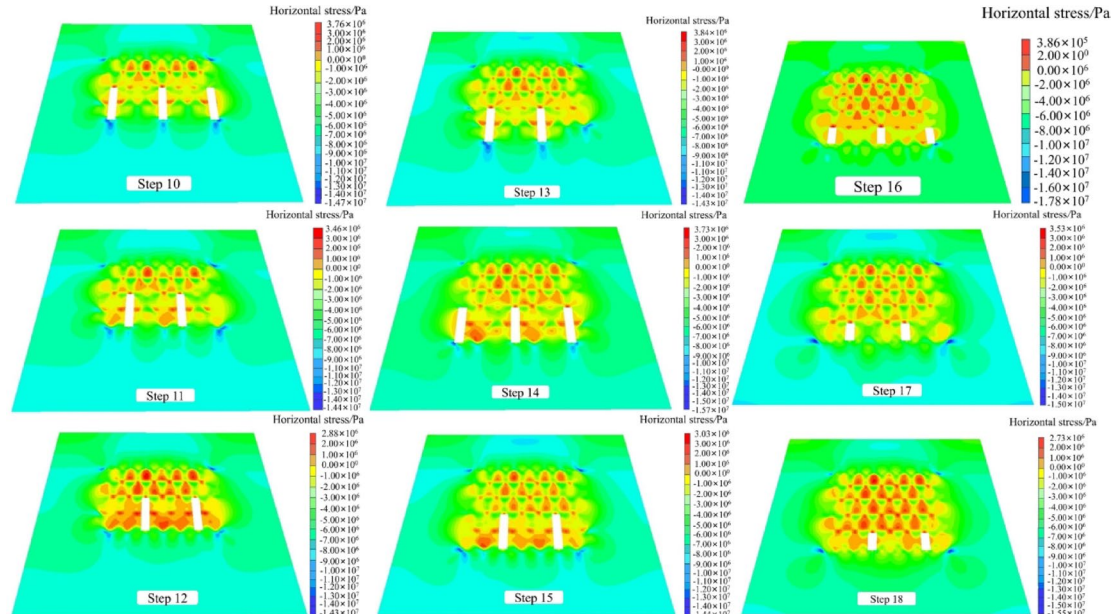


**Fig. 16.** Excavation steps 10–18 horizontal stresses.

tration area continues to expand, and the stress concentration area is mainly concentrated in the backfill and the roof and bottom plate of the mine house, and the stress concentration value of the backfill body is smaller than that of the roof and bottom plate of the mine house. In this case, all the values of the horizontal stress concentration area are negative, and the direction is the opposite direction of the z-axis. With the excavation steps 4–6, the stress concentration area does not expand significantly, but large stress concentration areas appear on both sides of the mining house. However, it is observed that extensive areas of concentration of stress emerge on both sides of the mining house. During the excavation process, from steps 7 to 9, the horizontal stress concentration area expands, and the horizontal stress concentration phenomenon occurs on both sides of the mine.

Figure 16 illustrates the horizontal stress variation diagram for steps 10–18 of the excavation process. As illustrated in Fig. 16, with the progress of the excavation steps, the horizontal stress concentration areas have appeared and are constantly expanding, and the horizontal stress concentration areas are mainly concentrated

in the areas that have been mined and filled and the surrounding areas of the mining houses. Concurrently, the horizontal stress concentration area is more extensive and the horizontal stress value is higher during the 10–12 steps of excavation. Additionally, the horizontal stress concentration area of some filling areas is interconnected. During the excavation steps 13–15, the horizontal stress concentration area continues to expand, and the backfill between the ore houses exhibits a pronounced stress concentration phenomenon. During the excavation steps 16–18, the horizontal stress concentration area of the entire model attains its maximum extent, with the greatest concentration occurring in the filling area and the surrounding rock.

The results of horizontal stress evolution show that the vertical stress shows a trend of concentrated expansion with the continuous progress of the excavation steps, and the local stress concentration phenomenon is relatively insignificant on the whole, and the initial stress in the excavation process is mainly concentrated in the backfill and the roof and bottom of the mine. In the middle stage of the excavation process, the horizontal stress is mainly concentrated in the area that has been mined and filled and the area around the mine house that is being mined. In the subsequent phase of the excavation process, the area of horizontal stress concentration continues to expand, with the backfill between the ore houses exhibiting a distinct stress concentration phenomenon. The horizontal stress is predominantly concentrated within the filling area and the surrounding rock, with an overall effective control of ground pressure.

### Comparison of the results of numerical simulation and physical model tests

The conclusion regarding the agreement between the physical model's strain measurements and the numerical stress contours is supported by the fundamental constitutive relationship used in the simulation. The numerical simulation employs the Mohr-Coulomb elastoplastic constitutive model, which intrinsically couples the stress state with the development of plastic strain through its yield criterion. This intrinsic relationship thereby ensures a close spatial correspondence between the high-stress zones predicted by the simulation and the large-strain zones observed in the physical experiments. This observed alignment provides strong, albeit indirect, validation that the numerical model is accurately replicating the internal mechanical response of the physical model, as the simulated stress fields are the direct computational result of the deformation patterns that the physical model visually exhibits.

As seen in Fig. 17, according to the numerical simulation horizontal stress cloud diagram, the surrounding rock on both sides of the excavation area is under compressive stress, and there is stress concentration. Based on the direction of compressive stress, it can be determined that the surrounding rock on both sides tends to move towards the excavation area. In addition, the horizontal strain values range from  $4.9 \times 10^{-3}$ ~ $5.6 \times 10^{-3}$  on both sides of the horizontal strain contour diagram of the physical model test, which can be judged to be consistent with the numerical simulation of the horizontal stress contour diagram according to the strain direction, which proves the consistency between the numerical simulation and physical model test.

In addition, according to Fig. 17, after excavation and filling, the horizontal strain of the surrounding rock on both sides of the excavation area is negative, the value is small, and the distribution area is small, which indicates that the high ground stress of the surrounding rock during excavation has been well controlled.

As seen in Fig. 18, according to the vertical stress cloud of the numerical simulation analysis, there are obvious stress concentrations on both sides and below the excavation area after the completion of excavation and backfilling, especially the concave compressive stress below the excavation area, which coincides with the vertical strain in the negative direction below the excavation area of the physical model test, which also proves the consistency between the numerical simulation and physical model test.

In addition, Fig. 18(a) shows that there are vertical stress concentrations in the surrounding rock on both sides of the stope excavation area, while the vertical strain on both sides of the excavation area in the vertical strain diagram of the physical model test is a small vertical strain, and the value range is between  $-5.2 \times 10^{-4}$  and  $-1.8 \times 10^{-3}$ , which is somewhat different.

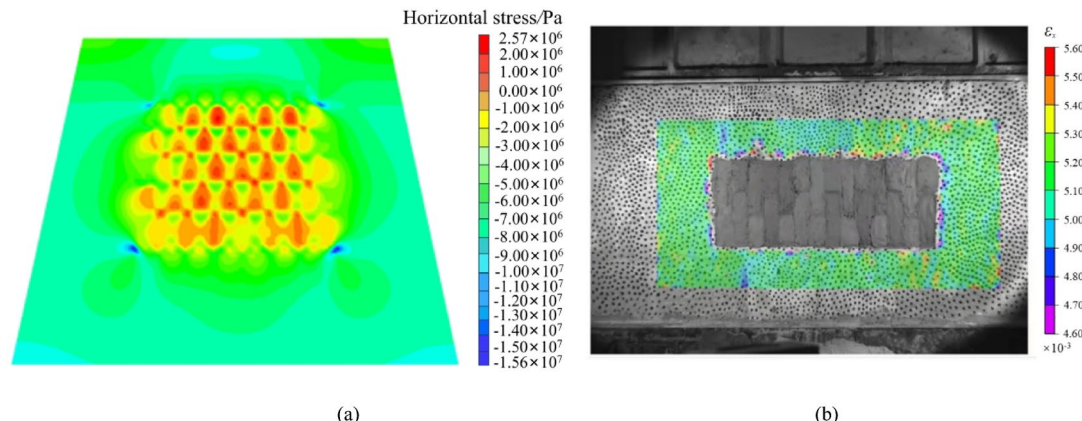


**Fig. 17.** Comparison of numerical simulation horizontal stress and similar simulation horizontal strain after completion of mining: (a) Numerical simulation horizontal stress cloud diagram; (b) Similar simulation horizontal strain cloud diagram.

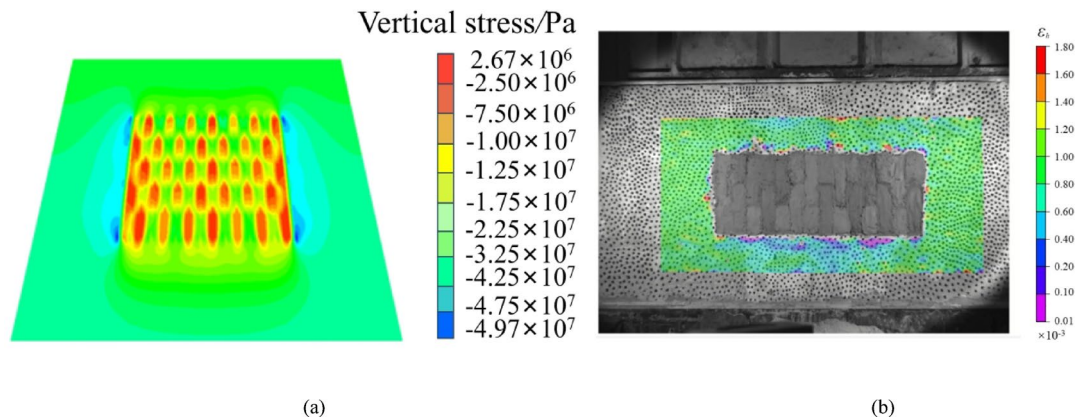


**Fig. 18.** Comparison of numerically simulated vertical stress and similar simulation vertical strain after mining is completed: (a) Numerical simulation vertical stress cloud diagram; (b) Similar simulation vertical strain cloud diagram.

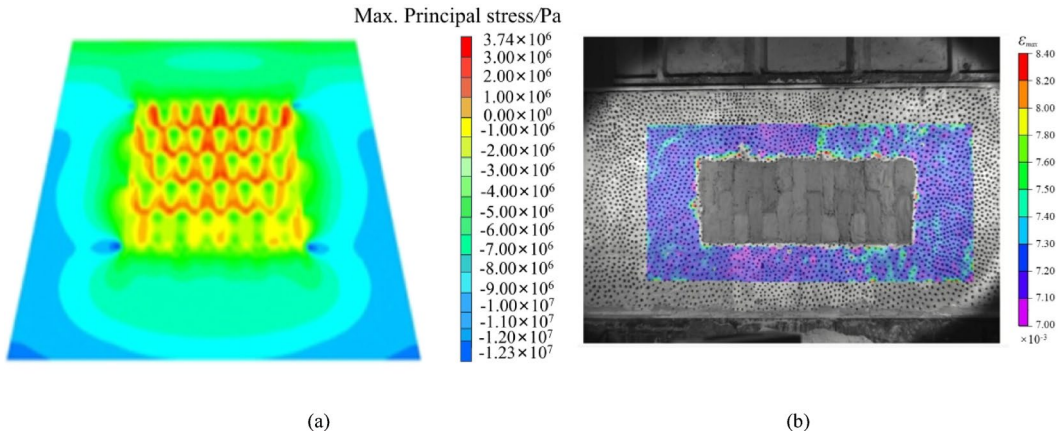


**Fig. 19.** Comparison of the maximum principal stress of the numerical simulation and the similar simulation maximum principal strain after the completion of mining: (a) Numerical simulation maximum principal stress cloud diagram; (b) Similar simulation maximum principal strain cloud diagram.

According to Fig. 18(b), the strain around the excavation area changes to a lesser extent after excavation and backfilling are completed, which indicates that the high ground stress in the surrounding rock is well controlled during the excavation process.

As shown in Fig. 19, according to the numerical simulation maximum principal stress distribution cloud diagram, the surrounding rock in the edge area of the numerical simulation model is mainly affected by compressive stress, while the edge of the excavation and filling area of the physical model test observes a positive maximum principal strain concentration with values ranging from  $7.0 \times 10^{-3}$  to  $8.4 \times 10^{-3}$ , indicating that this area is subject to compressive stress, which is consistent with the physical model test where the maximum principal strain is all in the negative direction. The test results are consistent with those of a physical model test where the maximum principal strain is in the negative direction.

Moreover, both the physical model test and the numerical simulation model are affected by compressive stresses in the parts outside the excavation area, and the results of the physical model test and the numerical simulation analysis are consistent.

As shown in Fig. 20, the surrounding rock at the edge of the numerical simulation is mainly affected by compressive stress, which coincides with the physical model test where the maximum principal strain at the edge of the excavation and filling area is in the negative direction.

From Fig. 20 (a) and Fig. 20 (b), the surrounding rock outside the excavation area is subjected to larger compressive stress, while in the area outside the excavation area of the physical model test, the left and right sides are affected by slight tensile stress, the top and bottom are more affected by compressive stress, and there is a certain difference between the two, but the results of the minimum principal strain (compressive stress) in the negative direction of the arc that exists below the mining area are in complete agreement.

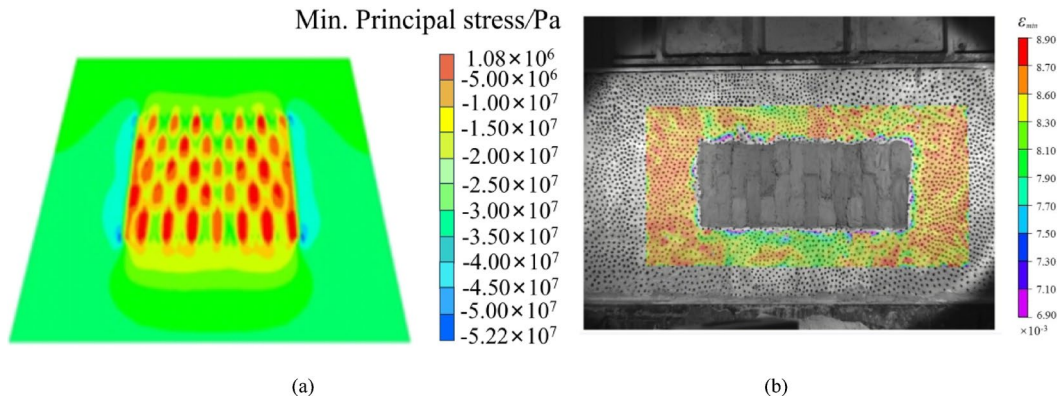


**Fig. 20.** Comparison of the minimum principal stress of the numerical simulation and the similar simulation minimum principal strain after the completion of mining: (a) Numerical simulation minimum principal stress cloud diagram; (b) Similar simulation minimum principal strain cloud diagram.

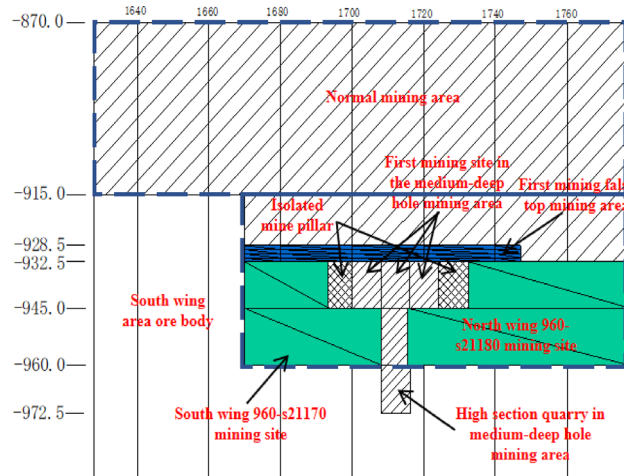


**Fig. 21.** Cross-section of the test stope.

### Engineering application and validation

The determined deep mining ground pressure control method was adopted for the field industrial test, and after the field research, the test area was selected between the 1600 line and 1800 line from the  $-915$  m to  $-975$  m level. The test area is divided into three zones: the first mining false top mining zone, the first mining site of the lower plate medium-deep hole and the high section mining site of the lower plate medium-deep hole. The specific test area is shown in Fig. 21. The industrial field test shows that the proposed ground pressure control method is scientific and reasonable, and the average production capacity of intelligent mining with medium-deep hole segmented empty field subsequent backfilling is 385 t/d, the mining loss rate is 7.62%, the mining depletion rate is 6.18%, and 53,400 t of ore is safely extracted during production at the test site. During the indicator calibration phase conducted in the experimental mining sector, a total of 53,400 metric tons of ore were successfully extracted under controlled safety conditions. The extracted material exhibited an average gold grade of 2.35 g/t, corresponding to a total contained metal content of 125.49 kg. Applying a metallurgical recovery rate of 94%, which reflects standard processing performance for this deposit type, the recoverable gold is calculated to be 117.96 kg. Based on the current gold price of 782.7 RMB/g, the potential gross revenue from metal sales is estimated at approximately 92.33 million RMB. Assuming project implementation proceeds as planned, with operating costs maintained within 430 RMB/t through optimized mining and processing strategies, the projected pre-tax profit would reach approximately 69.37 million RMB, demonstrating favorable economic viability for the mining method under evaluation. To facilitate a comparison of the medium and deep hole test area, the area of the Sanshandao gold mine was originally used by the approach method, with an average production capacity of 175t/d for the approach and fill mining method. Consequently, the production capacity has been increased from 175t/d to 385t/d of the original approach method, which has greatly improved the stope production capacity, and the field industrial test has achieved the expected results, which shows that the ground pressure control mining mode has certain promotion and application value, and possesses favourable engineering practicability.

## Study limitations and discussion

However, there are certain limitations to the study. Firstly, this study did not account for the influence of the  $F_1$  fault. Future work would benefit from a detailed investigation into the fault's effects, particularly by examining the spatial relationships between the fault, backfill, and surrounding rock mass. And the guidance provided by the new model in relation to engineering applications is a challenging area of investigation. Secondly, this paper focuses on the ground pressure regulation techniques employed in the deep mining of subsea gold deposits at the Sanshandao mine. Further studies on the general adaptability of the new ground pressure control mode could be conducted by analysing the results of similar deep mining operations at other metal mines. Besides, the detachment of strain gauges at locations 14–16 during the experiment resulted in the loss of strain data from these critical zones, particularly in the vicinity of the  $F_1$  fault. This gap potentially limits a complete understanding of the local strain field and its evolution during the failure process. To solve this limitation, the strain fields in these regions can be reasonably interpreted by combining numerical simulation results with data from adjacent functional strain gauges in future studies. Furthermore, a synthesis of the regulations governing the novel ground pressure control mode in deep mining could provide more comprehensive guidance for future deep mining operations.

## Conclusion

- (1) The results of the numerical simulation indicate that the vertical stress is relatively minor throughout the excavation process, with a relatively uniform stress distribution and insignificant local stress concentration. Nevertheless, as the excavation process continues, the horizontal stress demonstrates a tendency towards concentrated expansion, with the local stress concentration phenomenon remaining relatively insignificant. The results of the numerical simulation demonstrate that the novel mining mode is effective in controlling ground pressure.
- (2) The analysis results of the physical model test show that the similar material model has an obvious disturbance to the surrounding area during the excavation process, and the strain value continues to increase as the disturbance gradually intensifies with continuous excavation. Meanwhile, the backfilling of the extraction area helps to control the further development of the strain at the monitoring points around the excavation area, which indicates the good effect of the backfilling body on ground pressure control. In addition, the strain values at the monitoring points are approximately one in ten thousand, indicating that this ground pressure regulation mining method has a good control effect on the high ground stress.
- (3) The field industrial test shows that the production capacity of continuous mining after filling in the downwards directional segmented vacant field in the lower plate reaches 385 t/d, the mining loss rate is 7.62%, the mining depletion rate is 6.18%, and 53,400 t of ore is safely extracted during production at the test site, which also shows that the ground pressure control method is reasonable and effective. This method can be effectively applied to subsea and deep underground mining, where it demonstrates a significant capability in optimizing stress distribution and mitigating hazardous stress concentrations, thereby enhancing overall geomechanical stability.

## Data availability

The datasets used and analysed during the current study available from the corresponding author on reasonable request.

Received: 30 September 2024; Accepted: 9 December 2025

Published online: 23 December 2025

## References

- Bindler, R., Renberg, I., Rydberg, J. & Andrén, T. Widespread waterborne pollution in central Swedish lakes and the Baltic sea from pre-industrial mining and metallurgy. *Environ. Pollut.* **157**, 2132–2141. <https://doi.org/10.1016/j.envpol.2009.02.003> (2009).
- Zhang, F., Ti, Z. & Zhang, A. Simulation of impact stability test model in underwater coal mining of dam. *J. Coastal Res.* **642**–645. <https://doi.org/10.2112/SI83-106.1> (2018).
- Liu, W. J., Liu, Z. X., Wang, M. & Zhang, S. X. A comparative performance study on the development of hybrid extreme gradient boosting models for predicting rock layer subsidence in subsea gold mine. *Geomech. Geophys. GEO-ENERGY GEO-RESOURCES.* **11** <https://doi.org/10.1007/s40948-024-00912-4> (2025).
- Liang, W., Zhao, G., Wu, H. & Chen, Y. Optimization of mining method in subsea deep gold mines: A case study. *Trans. Nonferrous Met. Soc. China.* **29**, 2160–2169. [https://doi.org/10.1016/s1003-6326\(19\)65122-8](https://doi.org/10.1016/s1003-6326(19)65122-8) (2019).
- Peng, K., Li, X., Wan, C., Peng, S. & Zhao, G. -y. Safe mining technology of undersea metal mine. *Trans. NONFERROUS Met. Soc. CHINA.* **22**, 740–746. [https://doi.org/10.1016/s1003-6326\(11\)61239-9](https://doi.org/10.1016/s1003-6326(11)61239-9) (2012).
- Li, G. et al. A Case Study on Deformation Failure Characteristics of Overlying Strata and Critical Mining Upper Limit in Submarine Mining. *WATER* **14**. <https://doi.org/10.3390/w14162465> (2022).
- Wang, C. J., Liu, D. H., Chen, J. J., Li, C. L. & Yu, Y. Preliminary Assessment of Environmentally Friendly Mining Options Based on Various Mineral Resources-A Case Study of the Clarion-Clipperton Fracture Zone in Pacific. *SUSTAINABILITY* **16**. <https://doi.org/10.3390/su16177872> (2024).
- Davidsen, J. & Kwiatek, G. Earthquake interevent time distribution for induced Micro-, Nano-, and picoseismicity. *Phys. Rev. Lett.* **110** <https://doi.org/10.1103/PhysRevLett.110.068501> (2013).
- Mutshafa, N. et al. Seismic imaging of the gold deposit and geological structures through reprocessing of legacy seismic profiles near Kloof-Driefontein complex East Mine, South Africa. *Geophys. Prospect.* **71**, 1181–1196. <https://doi.org/10.1111/1365-2478.13283> (2023).
- Chen, Y., Zhao, G., Wang, S., Wu, H. & Wang, S. A case study on the height of a water-flow fracture zone above undersea mining: Sanshandao gold Mine, China. *Environ. Earth Sci.* **78** <https://doi.org/10.1007/s12665-019-8121-7> (2019).

11. Liu, Z. et al. Construction of reasonable pillar group for undersea mining in metal mine. *Trans. Nonferrous Met. Soc. China.* **28**, 757–765. [https://doi.org/10.1016/s1003-6326\(18\)64708-9](https://doi.org/10.1016/s1003-6326(18)64708-9) (2018).
12. Chai, J., Du, W., Yuan, Q. & Zhang, D. Analysis of test method for physical model test of mining based on optical fiber sensing technology detection. *Opt. Fiber. Technol.* **48**, 84–94. <https://doi.org/10.1016/j.yofte.2018.12.026> (2019).
13. Darvishi, A., Ataei, M. & Rafiee, R. Investigating the effect of simultaneous extraction of two Longwall panels on a maingate gateroad stability using numerical modeling. *Int. J. Rock Mech. Min. Sci.* **126** <https://doi.org/10.1016/j.ijrmms.2019.104172> (2020).
14. Li, X. B., Wang, D. Y., Li, C. J. & Liu, Z. X. Numerical simulation of surface subsidence and backfill material movement induced by underground mining. *Adv. CIVIL Eng.* **2019** <https://doi.org/10.1155/2019/2724370> (2019).
15. Wang, F., Chen, S. J., Xu, J. L. & Ren, M. Z. New Method to Design Coal Pillar for Lateral Roof Roadway Based on Mining-Induced Stress: A Case Study. *ADVANCES IN CIVIL ENGINEERING* **2018**. <https://doi.org/10.1155/2018/4545891> (2018).
16. Fang, F., Shu, C. & Wang, H. Physical simulation of upper protective coal layer mining with different coal seam inclinations. *ENERGY Sci. Eng.* **8**, 3103–3116. <https://doi.org/10.1002/ese3.740> (2020).
17. Cheng, Q., Shi, Y. K. & Zuo, L. Q. Numerical simulation and analysis of surface and surrounding rock failure in deep High-Dip coal seam mining. *Geotech. Geol. Eng.* **37**, 4285–4299. <https://doi.org/10.1007/s10706-019-00907-z> (2019).
18. Wang, Y. Q. et al. Roof Subsidence and Movement Law of Composite Strata Mining: Insights from Physical and Numerical Modeling. *MINERALS* **12**. <https://doi.org/10.3390/min12010003> (2022).
19. Li, W. X. et al. A visco-elastic theoretical model for analysis of dynamic ground subsidence due to deep underground mining. *Appl. Math. Model.* **39**, 5495–5506. <https://doi.org/10.1016/j.apm.2015.01.003> (2015).
20. Zheng, K., Xuan, D. & Li, J. Study on Fluid-Solid characteristics of grouting filling Similar-Simulation materials. *MINERALS* **12** <https://doi.org/10.3390/min12050502> (2022).
21. Cui, F., Jia, C. & Lai, X. Study on deformation and energy release characteristics of overlying strata under different mining sequence in close coal seam group based on similar material simulation. *ENERGIES* **12** <https://doi.org/10.3390/en12234485> (2019).
22. Li, X., Geng, J., Li, Q., Tian, W. & Zhou, T. Behaviors and overlying strata failure law for underground filling of a gently inclined Medium-Thick phosphate deposit. *Adv. CIVIL Eng.* **2021** <https://doi.org/10.1155/2021/3275525> (2021).
23. Li, X., Qiu, J., Zhao, Y., Chen, Z. & Li, D. -y. Instantaneous and long-term deformation characteristics of deep room-pillar system induced by pillar recovery. *Trans. NONFERROUS Met. Soc. CHINA.* **30**, 2775–2791. [https://doi.org/10.1016/S1003-6326\(20\)65420-6](https://doi.org/10.1016/S1003-6326(20)65420-6) (2020).
24. Liu, Z., Dang, W. & He X.-g. Undersea safety mining of the large gold deposit in Xinli district of Sanshandao gold mine. *Int. J. MINERALS Metall. Mater.* **19**, 574–583. <https://doi.org/10.1007/s12613-012-0598-y> (2012).
25. Lu, M., Sun, X., Xiao, Y. & Zhang, C. The development mining-induced surface cracks in shallow coal seam through double-gully terrain: a case study in a coal mine. *Bull. Eng. Geol. Environ.* **81** <https://doi.org/10.1007/s10064-022-02882-x> (2022).
26. Liu, Z., Han, K., Yang, S. & Liu, Y. -x. Fractal evolution mechanism of rock fracture in undersea metal mining. *J. Cent. SOUTH. Univ.* **27**, 1320–1333. <https://doi.org/10.1007/s11771-020-4369-z> (2020).
27. Xu, H. et al. Energy dissimilation characteristics and shock mechanism of coal-rock mass induced in steeply-inclined mining: comparison based on physical simulation and numerical calculation. *Acta Geotech.* **18**, 843–864. <https://doi.org/10.1007/s11440-022-01617-2> (2023).
28. Wang, Y. Q. et al. Similar experimental study on retaining waterproof coal pillar in composite strata mining. *Sci. Rep.* **12** <https://doi.org/10.1038/s41598-022-05369-7> (2022).
29. Zhang, J. W., Wang, Z. W. & Song, Z. X. Numerical study on movement of dynamic strata in combined open-pit and underground mining based on similar material simulation experiment. *Arab. J. Geosci.* **13** <https://doi.org/10.1007/s12517-020-05766-0> (2020).
30. Lv, W., Guo, K., Yu, J., Du, X. & Feng, K. Surrounding rock movement of steeply dipping coal seam using backfill mining. *SHOCK Vib.* **2021** <https://doi.org/10.1155/2021/5574563> (2021).
31. Li, A. et al. Physical simulation study on grouting water plugging of flexible isolation layer in coal seam mining. *Sci. Rep.* **12** <https://doi.org/10.1038/s41598-022-04813-y> (2022).
32. Zhang, S. et al. Physical simulation on weakly cemented aquiclude stability due to underground coal mining. *MINERALS* **12** <https://doi.org/10.3390/min12121494> (2022).
33. Qiu, J. et al. Physical model test on the deformation behavior of an underground tunnel under blasting disturbance. *Rock Mech. Rock Eng.* **54**, 91–108. <https://doi.org/10.1007/s00060-020-02249-2> (2021).
34. Li, Y. et al. Stress evolution and failure characteristics of overburden during Multi-Stop mining for a gently inclined thin orebody. *Min. Metall. Explor.* **40**, 637–653. <https://doi.org/10.1007/s42461-023-00746-w> (2023).
35. Ma, C., Yuan, Y., Zha, J., Li, H. & Xu, Y. Determine method of effective experimental period of similar material model for improving the simulation results. *ENERGY SOURCES PART. A-RECOVERY UTILIZATION Environ. Eff.* <https://doi.org/10.1080/15567036.2020.1815909> (2020).
36. Shi, Y., Ye, Y., Hu, N., Jiao, Y. & Wang, X. Physical simulation test on surrounding rock deformation of roof rockburst in continuous tunneling roadway. *MINERALS* **11** <https://doi.org/10.3390/min11121335> (2021).
37. Zhou, Z. et al. Experimental investigation of the progressive failure of multiple Pillar-Roof system. *Rock Mech. Rock Eng.* **51**, 1629–1636. <https://doi.org/10.1007/s00603-018-1441-1> (2018).
38. Zhou, T., Zhu, J. & Xie, H. Mechanical and volumetric fracturing behaviour of Three-Dimensional printing Rock-like samples under dynamic loading. *Rock Mech. Rock Eng.* **53**, 2855–2864. <https://doi.org/10.1007/s00603-020-02084-5> (2020).
39. Zhu, G. Q. et al. Real-time monitoring of the development of brittle fracture in hard rock tunnels based on physical model test. *Tunn. Undergr. Space Technol.* **119** <https://doi.org/10.1016/j.tust.2021.104240> (2022).
40. Hai-feng, L., Kai, Z. & Jin-long, Y. Ai-chao, W. A study on the optimal selection of similar materials for the physical simulation experiment based on rock mineral components. *Eng. Fail. Anal.* **140** <https://doi.org/10.1016/j.englfailanal.2022.106607> (2022).
41. Nie, B., Gu, S. & Zeng, S. Similarity criteria of water drive physical simulation of Pressure-Sensitive fractured reservoirs. *GEOFLOIDS* **2021** <https://doi.org/10.1155/2021/5042656> (2021).
42. Wu, Y., Liu, M., Xie, P., Wang, H. & Hu, B. Three-Dimensional physical similarity simulation experiments for aTransparent shaft coal pocket wall in coal mines. *ACS OMEGA.* **7**, 16442–16453. <https://doi.org/10.1021/acsomega.2c00450> (2022).
43. Shi, Y., Ye, Y., Hu, N., Huang, X. & Wang, X. Experiments on material proportions for similar materials with high similarity ratio and low strength in multilayer shale deposits. *Appl. SCIENCES-BASEL.* **11** <https://doi.org/10.3390/app11209620> (2021).
44. Liu, W. J., Liu, Z. X., Xiong, S. & Wang, M. Comparative prediction performance of the strength of a new type of Ti tailings cemented backfilling body using PSO-RF, SSA-RF, and WOA-RF models. *CASE Stud. Constr. Mater.* **20** <https://doi.org/10.1016/j.cscm.2023.e02766> (2024).
45. Sun, W., Zhou, F., Shao, J., Du, H. & Xue, Y. c. Development status and prospects of mine physical similar material simulation experiments. *Geotech. Geol. Eng.* **37**, 3025–3036. <https://doi.org/10.1007/s10706-019-00821-4> (2019).
46. Chen, B., Zhang, S., Li, Y., Li, Z. & Zhou, H. Physical simulation study of crack propagation and instability information discrimination of rock-like materials with faults. *Arab. J. Geosci.* **13** <https://doi.org/10.1007/s12517-020-05966-8> (2020).
47. Liu, W., Liu, Z. & Liu, Z. Prediction of strata settlement in undersea metal mining based on deep forest. *Sci. Rep.* **14** <https://doi.org/10.1038/s41598-024-80025-w> (2024).
48. Zhou, X. P. & Wang, Y. T. Numerical simulation of crack propagation and coalescence in pre-cracked rock-like Brazilian disks using the non-ordinary state-based peridynamics. *Int. J. Rock Mech. Min. Sci.* **89**, 235–249. <https://doi.org/10.1016/j.ijrmms.2016.09.010> (2016).

49. Son, M. & Cording, E. J. Numerical model tests of Building response to excavation-induced ground movements. *Can. Geotech. J.* **45**, 1611–1621. <https://doi.org/10.1139/T08-074> (2008).
50. Liu, W., Liu, Z. & Li, Z. Study on optimization of downward mining schemes of Sanshandao gold mine. *Appl. Sci.* **15** <https://doi.org/10.3390/app15158296> (2025).

## Acknowledgements

The authors thank the anonymous reviewers for their helpful and constructive comments.

## Author contributions

W.L.: ideas and methods, methodology, writing—original draft; Z.L.: investigation, data curation, writing—review and editing, supervision, resources, funding acquisition, project administration; J. Q.: software, provide guidance for the experiment; T.G.: participate in experiments, validation, investigation; Q.Z.: writing—review and editing, supervision, resources, funding acquisition. All authors reviewed the manuscript.

## Funding

This work was supported by the National Natural Science Foundation of China (No. 52374107, 52304091 and 52304113), the Fundamental Research Funds for the Central Universities of Central South University (2024zzts0421) and the Research Project of Education Department of Hunan Province (No. 22B0427).

## Declarations

### Competing interests

The authors declare no competing interests.

### Additional information

**Supplementary Information** The online version contains supplementary material available at <https://doi.org/10.1038/s41598-025-32253-x>.

**Correspondence** and requests for materials should be addressed to Q.Z.

**Reprints and permissions information** is available at [www.nature.com/reprints](http://www.nature.com/reprints).

**Publisher's note** Springer Nature remains neutral with regard to jurisdictional claims in published maps and institutional affiliations.

**Open Access** This article is licensed under a Creative Commons Attribution-NonCommercial-NoDerivatives 4.0 International License, which permits any non-commercial use, sharing, distribution and reproduction in any medium or format, as long as you give appropriate credit to the original author(s) and the source, provide a link to the Creative Commons licence, and indicate if you modified the licensed material. You do not have permission under this licence to share adapted material derived from this article or parts of it. The images or other third party material in this article are included in the article's Creative Commons licence, unless indicated otherwise in a credit line to the material. If material is not included in the article's Creative Commons licence and your intended use is not permitted by statutory regulation or exceeds the permitted use, you will need to obtain permission directly from the copyright holder. To view a copy of this licence, visit <http://creativecommons.org/licenses/by-nc-nd/4.0/>.

© The Author(s) 2025